X-ray diffraction study of phase transformation dynamics of Fe and Fe-Si alloys along the shock Hugoniot using an x-ray free electron laser

A. Krygier, M. Harmand, B. Albertazzi, E. Mcbride, K. Miyanishi, Daniele Antonangeli, Y. Inubushi, R. Kodama, M. Koenig, T. Matsuoka, et al.

X-ray diffraction study on phase transformation dynamics of iron and Fe-Si alloys along the shock Hugoniot using an x-ray free electron laser

A. Krygier,[1,2,*] M. Harmand,[1] B. Albertazzi,[3] E. E. McBride,[4,5] K. Miyanishi,[6,7] D. Antonangeli,[1] Y. Inubushi,[7,8] R. Kodama,[6,9] M. Koenig,[3,9] T. Matsuoka,[10] G. Mogni,[1] F. Pietrucci,[1] A. M. Saitta,[1] T. Togashi,[7,8] Y. Umeda,[9,11] T. Vinci,[3] M. Yabashi,[7,8] T. Yabuuchi,[7,8] G. Fiquet,[1] and N. Ozaki[6,9]

[1]*Sorbonne Université, Muséum National d'Histoire Naturelle, UMR CNRS 7590, Institut de Minéralogie, de Physique des Matériaux, et de Cosmochimie (IMPMC), 75005 Paris, France*
[2]*Lawrence Livermore National Laboratory, 7000 East Ave, Livermore, CA 94550, USA*
[3]*LULI, CNRS, CEA, Sorbonne Université, Ecole Polytechnique, Institut Polytechnique de Paris, F-91120 Palaiseau cedex, France*
[4]*European XFEL GmbH, Holzkoppel 4, D-22869 Schenefeld, Germany*
[5]*SLAC National Accelerator Laboratory, 2575 Sand Hill Road, MS 19, Menlo Park, California 94025, USA*
[6]*Institute for Laser Engineering, Osaka University, Suita, Osaka 565-0871, Japan*
[7]*RIKEN Spring-8 Center, Sayo, Hyogo 679-5148, Japan*
[8]*Japan Synchrotron Radiation Research Institute, Sayo, Hyogo 679-5198, Japan*
[9]*Graduate School of Engineering, Osaka University, Suita, Osaka 565-0871, Japan*
[10]*Open and Transdisciplinary Research Initiatives, Osaka University, Suita, Osaka 565-0871, Japan*
[11]*Institute for Integrated Radiation and Nuclear Science, Kyoto University, Sennan, Osaka 590-0494, Japan*

(Dated: June 2, 2022)

The x-ray free electron laser (XFEL) enables probing highly compressed material response at the sub-nanosecond timescale. We exploit the ultrafast XFEL pulse to combine reflection x-ray diffraction and laser-driven shock compression to perform a study of phase transformation and stability in iron and Fe-Si alloys. Our approach enables us to observe that solid-solid phase transformations occur in iron and Fe-$Si_{8.5wt\%}$ in $\leq$130 ps at $\sim$130 GPa; no transformation is observed in Fe-$Si_{16wt\%}$ up to 110 GPa. Density Functional Theory calculations predict similar phase relations.

INTRODUCTION

High pressure and temperature properties of iron[1–6] and Fe-Si alloys[7–12] are important due to their prominence in geophysics, planetary science, and wide industrial use[13]. Iron is the main component of the core of telluric planets and Si is a potentially significant core alloy component for Earth, Mercury, and many exoplanets[14], in particular when formed under reducing conditions. Si is also a commonly used alloy element in high-performance steels and advanced magnetic materials[15]. The addition of Si is suggested to stabilize cubic phases over a large pressure and temperature range[16–19], at the expense of the hexagonally-close-packed (hcp) structure, the ε-phase of pure iron at high pressure. In iron, the transformation from ambient body-centered-cubic (bcc) to hcp phase is Martensitic and thus a rapid transformation. Despite significant effort, much about these materials remains unknown.

X-ray diffraction (XRD) measurements of Fe-Si alloys compressed using diamond anvil cells (DAC) and Laser Heated DAC (LH-DAC)[12,16,17,19–22] show disagreement. Hirao et al.[20] report that Fe-$Si_{8.7wt\%}$ transforms from ambient bcc-phase to hcp over pressures $\sim$16-35 GPa while the cubic phase remains stable in Fe-$Si_{17.8wt\%}$ up to $\sim$124 GPa (300 K). Fischer et al.[17] report that Fe-$Si_{9wt\%}$ transforms from cubic to hcp-phase around 45 GPa/1400 K, and suggest a phase boundary at $\sim$20 GPa/1000 K, with a B2-hcp mixture at higher temperature, up to melting. Fischer et al.[16] report that Fe-$Si_{16wt\%}$ transforms from cubic B2 or $D0_3$ phase to mixed B2-hcp phase above 50 GPa/1000 K. Edmund et al.[19] investigated the Si concentration dependence of the bcc-hcp transformation pressure and find an increase of $\sim$11.5 GPa/wt% Si between $\sim$8-12 wt% at 300 K and that the cubic phase remains stable in Fe-$Si_{17wt\%}$ up to $\sim$65 GPa. Wicks et al.[18] explored phase relations in iron, Fe-$Si_{7wt\%}$ and Fe-$Si_{15wt\%}$ phase relations up to 1300 GPa using ramp compression and nanosecond XRD. Unlike Fischer[17] and consistent with Edmund[19] they observe no phase transformation in Fe-$Si_{15wt\%}$, possibly due to the lower temperature or the short timescale preventing dissociation into Si-rich B2 and Si-poor hcp. Despite the numerous studies and strong dependence of mechanical properties on crystalline structure[4,23–25], the phase diagrams of Fe-Si alloys remain uncertain.

While static compression with DAC is widely used in high pressure experiments, there are some drawbacks. These include limits on pressure and temperature, diffuse contamination of carbon from the anvil[3,26], formation of preferred crystallite orientations[27], and the frequent need for a pressure scale[28,29]. Sample de-mixing can also occur from pressure and temperature-induced solubility changes[30,31].

On the other hand, laser-driven dynamic compression can achieve very high pressures and temperatures and sample composition is not likely to be impacted by diffusion due to the timescale. However, the x-ray sources typically available at laser-driven dynamic compression facilities are uncollimated and of nanosecond duration[32]. High-power lasers coupled to femtosecond XFEL sources now produce very high quality XRD of dynamically compressed samples[33–38].

In laser-driven dynamic compression, an expanding plasma drives a pressure wave into the sample, creating $\sim$1-10s nanosecond-duration high-pressure states at strain rates up to $\sim 10^9$ s^{-1}. Though the initial strain is uniaxial, the sample rapidly approaches hydrostaticity through plasticity, phase

transformation, or twinning[39], etc. A benefit of this approach is precise knowledge of the *in-situ* sample composition, however, interpretation of results can be complicated by kinetic effects[15,40,41]. Smith et al.[5] and Amadou et al.[41] inferred that the bcc-hcp transformation occurs on the ∼1 ns timescale in pure iron and find a higher transformation onset stress than in static compression; kinetics in non-metals can occur on longer timescales[33,42]. Recent measurements also report phase transformation boundary lowering in dynamic compression[36,37].

RESULTS

We use the ∼10 fs x-ray pulse at the Spring-8 Angstrom Compact Free Electron Laser[43–45] (SACLA) facility to determine the crystal structure in compressed iron, Fe-$Si_{8.5wt\%}$, and Fe-$Si_{16wt\%}$. Every experiment uses the same laser pulse shape and general sample design. The Paylene-N ablator is coated directly onto the iron or Fe-Si layer, ensuring the shock state is not altered by reverberations from glue layers. The pulse duration, sample design, and geometry allow us to observe rapid onset of hcp-phase in iron and Fe-$Si_{8.5wt\%}$ during the initial shock and no structural transformation in Fe-$Si_{16wt\%}$ during the initial shock or on release, in disagreement with some early static measurements[16,17].

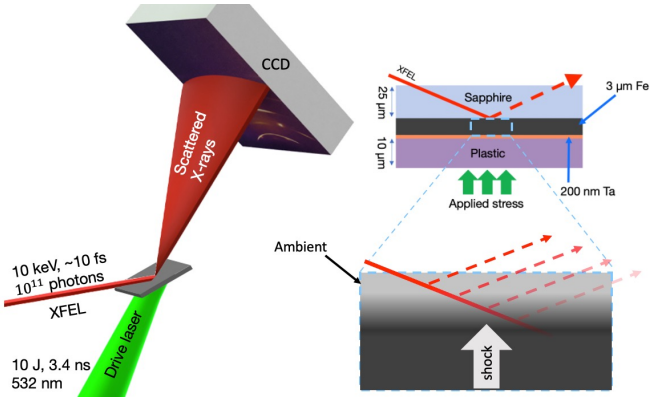

FIG. 1. Experimental configuration. The sample and probe geometry are detailed in the top right inset. The bottom right inset is a sketch highlighting the probe sensitivity to traveling shock wave. The large incidence angle highly biases the probed volume to the rearmost 1μm of the sample; this distance corresponds to the distance a shock wave in our conditions travels in ∼130 ps.

Figure 2 (a) and (b) show raw XRD images from ambient and compressed iron, respectively. The highly textured (preferred crystallite orientation) iron samples produce azimuthally narrow XRD spots, which prevents observation of some reflections, but enables exploitation of the known bcc-hcp orientation relationship[2,46]. Our analysis uses the textural similarity between the ambient and high-pressure diffraction. The high-pressure bcc {110} and {211} reflections in Fig. 2 (b) have the same pattern as their ambient counterparts in (a) and correspond to the same bcc lattice parameter to within ∼1%. We identify the hcp {002} reflection (Fig. 2 (b), red) by combining knowledge of the initial bcc texture and *a priori* knowledge of the parent-child orientation relationship where the atoms comprising the bcc {110} plane become the hcp {002} plane, maintaining their initial orientation. This relationship combined with their similar d-spacings for our pressure produces the similar azimuthal bcc {110} and hcp {002} diffraction patterns.

Figure 3 shows integrated XRD patterns of ambient (dashed green line) and *in situ* high-pressure (solid purple line) of iron (a), Fe-$Si_{8.5wt\%}$ (b), and Fe-$Si_{16wt\%}$ (c). Phase and corresponding reflection plane are labeled. Iron and Fe-$Si_{8.5wt\%}$ patterns include reflections from a ∼100 nm Au deposition to aid sample alignment (see Supplementary Material[47]). Across our data, the shock rise time is 0.5±0.1 ns, which combined with the directly measured strain gives a strain rate of $\dot{\varepsilon} = (V_0 - V)/V_0)/\Delta t = 5.9\times10^8$ s^{-1}, below the extrapolated value from Swegle-Grady[48] for our pressures.

The Fe-$Si_{8.5wt\%}$ samples (XRD image in Fig. 2 (c)) are textured differently than iron, but the implied lattice parameter from the bcc {110} and {211} reflections (Fig. 3 (b)) agree similarly, so we interpret the three reflections in the same way.

The Fe-$Si_{16wt\%}$ samples form the B2 structure at ambient conditions. Fischer et al.[16] report $D0_3$ structure at ambient conditions in similar samples, however, $D0_3$ and B2 are structurally alike with $D0_3$ producing several additional weak reflections that might be below the detection threshold. Furthermore, physical vapor deposition synthesis at relatively low temperature does not favor Si ordering[19,49]. The data in Fig. 3 were collected during the initial shock. We therefore expected to see a B2 + hcp mixture in our conditions.

DISCUSSION

We neither find evidence of structural phase transformation to the hcp-structure reported by Fischer, nor other possible Fe-Si structures[50–52]. This includes measurements made during the initial shock over a range of pressures (∼10-110 GPa) and after releasing into the sapphire window. The disappearance of weaker reflections at high pressure is due to the background and noise generated by the ablation plasma, but does not invalidate our conclusions: we cannot distinguish bcc from B2 or $D0_3$ (references to B2 phase observation have this caveat throughout) but we can clearly discard the presence of hcp phase. Wave profile measurements of shock- and ramp-compressed iron report kinetics associated with the bcc-hcp transformation[15,40,41] and simulations of shocked iron predict an elastic-plastic-transformation process[53–55]. Nevertheless, direct crystal structure measurements remain critical as the association between wave profile features and phase transformation must otherwise be assumed, which has been shown to be problematic in some materials[36].

Measuring x-ray diffraction with an XFEL and thin samples provides a nearly instantaneous snapshot of the crystallographic state - the ∼10 fs x-ray pulse and its time-of-flight across the sample are very short compared to hydrodynamic timescales. A 100 GPa shock in iron has a shock velocity of ∼ 7000 m/s meaning that the shock travels only ∼0.7 Å during

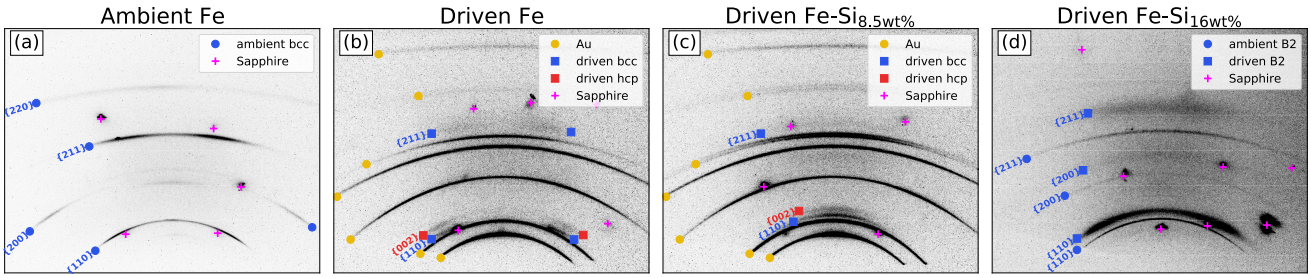

FIG. 2. Raw diffraction images of ambient iron (a), driven iron (b), driven Fe-$Si_{8.5wt\%}$ (c), and driven Fe-$Si_{16wt\%}$ (d). Circles (squares) indicate ambient (compressed) reflections. Gold circles indicate Au; pink pluses indicate sapphire. Blue and red markers indicate cubic (bcc/B2) and hcp phase reflections, respectively.

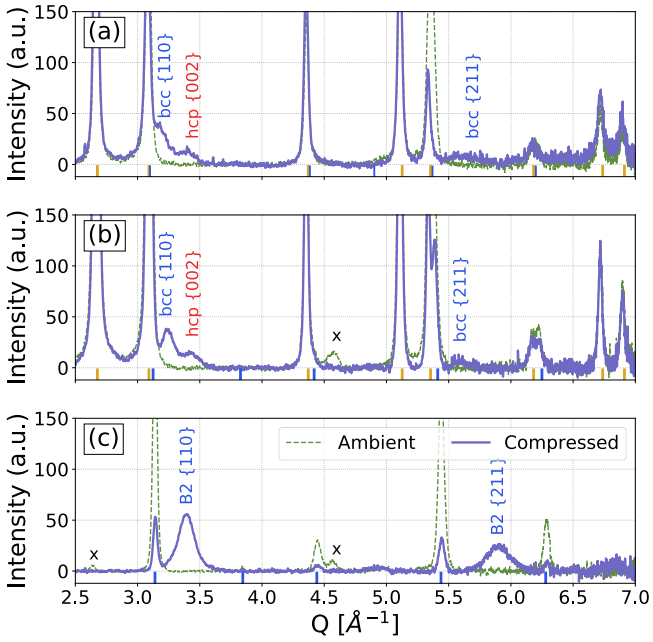

FIG. 3. Diffraction patterns of shocked iron (a), Fe-$Si_{8.5wt\%}$ (b), and Fe-$Si_{16wt\%}$ (c). Green (purple) curves denote ambient (compressed) samples. Gold (blue) ticks mark Au (ambient sample) reflections. Black x symbols indicate sample holder reflections; sapphire reflections are masked.

the x-ray pulse, less than the inner-atomic distance. The time-of-flight of the x-ray pulse in our sample is also very short. At 70° incidence, it takes only ∼30 fs to transit the ∼3 μm thick sample. During this time, the same 100 GPa shock travels only 2 Å, which is approximately the inner-atomic distance in iron in a 100 GPa shock. This is a clear advantage over synchrotron and laser-driven x-ray sources which have durations of 0.1-1 ns.

In our geometry, x-rays that contribute to the measured diffraction signal are incident on the rear surface and then reflected back through the same surface (see Fig. 1). This means that the path length through the sample rapidly increases with scattering depth and deeper parts of the sample contribute less signal due to stronger attenuation. This is different than the more common transmission geometry[37,38] where attenuation is more uniform with scattering depth. The reflection geometry therefore provides a comparatively strong rear-surface sensitivity. For example, the total path length in iron of an x-ray that diffracts from the ambient bcc {110} plane at a depth of 1 μm has a path length of ∼7 μm, similar to the attenuation length of 10.1 keV x-rays. Considering only attenuation in iron, 64% of detected x-rays are scattered from the rearmost 1 μm of the sample. It would be possible to tune this sensitivity in most materials by selecting an appropriate x-ray probe energy.

We exploit these factors to record x-ray diffraction of the leading edge of the shock. On some experiments, the x-ray probe is timed before the shock breaks out of the sample. In these cases, both ambient and compressed states contribute to the signal, the former confirming the position of the shock in the sample and the latter corresponding to the leading edge of the shock wave (bottom-right inset in Fig. 1). Again, considering only x-ray attenuation, this implies that any measured diffraction coming from the compressed sample is preferentially sensitive to the leading edge of the shock. In our conditions, a shock in iron travels 1 μm in ∼130 ps meaning that the signal from compressed iron corresponds to the evolution of the shock on that timescale.

The simultaneous observation of compressed bcc and hcp phases is consistent with the transient compression dynamics described by Kadau[53–55]. The observation of hcp-phase in the leading edge of the shock effectively sets an upper bound of ∼130 ps on the bcc-hcp phase transformation onset in iron and Fe-$Si_{8.5wt\%}$ under these conditions. This time resolution also allows us to confirm the inconsistency in the various phase diagrams proposed for Fe-$Si_{16wt\%}$[17–19] and to propose a possible explanation for this disagreement below.

The d-spacing of the transient, compressed iron bcc phase corresponds to hydrostatic pressure of 19.1±6.6 GPa (Sesame 2150), though the conditions inside the shock front are not at equilibrium and our data is not sensitive to possible structural anisotropy associated with an elastic wave or strength. The {002} hcp d-spacing corresponds to hydrostatic pressure of 128±35 GPa. The pressure of the final state is well above the expected hcp onset stress determined by Smith et

al. ($\sigma_{\alpha\to\varepsilon} = 1.15 \times \dot{\varepsilon}^{0.18}$) that evaluates to 44 GPa in our conditions, and so we would expect to observe hcp. The nature and dynamics of the initial compression remains an open and interesting question for future, tailored dynamic compression studies.

Hwang et al.[56] have also investigated shocked iron on subnanosecond timescales, however, their results are difficult to interpret. Their calculated strain rate is significantly higher than expected for their shock pressures[48] and they report a significantly larger Hugoniot elastic limit (HEL) than previously observed[40], though how the HEL is identified is not clear. Temporal and spatial gradients may be important due to very short pulse length ($\sim$ 140 ps) and small laser focus (40 μm full-width at half-maximum Gaussian focus vs. 20 μm XFEL probe area). How these effects impact the sampled hydrodynamic state is not easily discerned by argument and not addressed with measurements or multi-dimensional hydrodynamics simulations. Unlike Hwang et al., we do not observe multiple features associated with compressed bcc, which may be due to the higher pressure in our iron experiments and/or lower susceptibility to gradients.

Our results highlight the importance of investigating phase transformation dynamics in compression experiments before applying the results to constrain phase diagrams. They also highlight the advantage of using textured samples[39,57,58] for this purpose, and could be especially useful for identifying phase transformation orientation relationships and kinetics. Performing this experiment with a powder sample could hypothetically lead to incorrectly identifying the driven bcc {110} reflection as the hcp {100} plane. This would incorrectly yield a c/a ratio of 1.64 for the hcp phase, which is significantly higher than observed in either dynamic[59] or static[60] experiments, and could have misleading geophysical implications[61–63].

The reflections observed during the initial shock in Fe-Si$_{8.5\text{wt\%}}$ are similar to iron, suggesting similar interpretation and underlying phenomena. The transient bcc{110} and {211} d-spacings correspond to 38 GPa hydrostatic pressure; the high-pressure hcp {002} corresponds to 132$\pm$26 GPa pressure (using Hirao et al.[20]). We make no thermal corrections since the Hirao data agrees well with the Fe-Si$_{6.9\text{wt\%}}$ shock Hugoniot data from Marsh et al.[64] (Fig. 4); measurements of Fe-Si$_{5\text{wt\%}}$ at slightly lower pressure[14] suggest the thermal pressure is $\sim$15 GPa for our conditions, similar to that found by Fischer et al. in Fe-Si$_{16\text{wt\%}}$ and less than our error bars. The inferred bcc pressure is consistent with our calculations for the transformation pressure described below. Given the rapid onset, this transformation in Fe-Si$_{8.5\text{wt\%}}$ is likely a non-diffusive process like iron's Martensitic bcc-hcp phase transformation.

Conversely, we do not observe phase transformation in Fe-Si$_{16\text{wt\%}}$. This disagrees with Fischer et al.[16], but agrees with Edmund et al.[19] at room temperature and and ramp compression data from Wicks et al.[18] at moderate temperature.

Finally, we performed 0 K structural prediction calculations using Density Functional Theory (DFT). Predicted phases between 0 and 120 GPa for Fe-Si$_{9.1\text{wt\%}}$ ($Fe_{10}Si_2$) and Fe-Si$_{16.7\text{wt\%}}$ ($Fe_{10}Si_4$ or Fe_5Si_2) were calculated by estimating

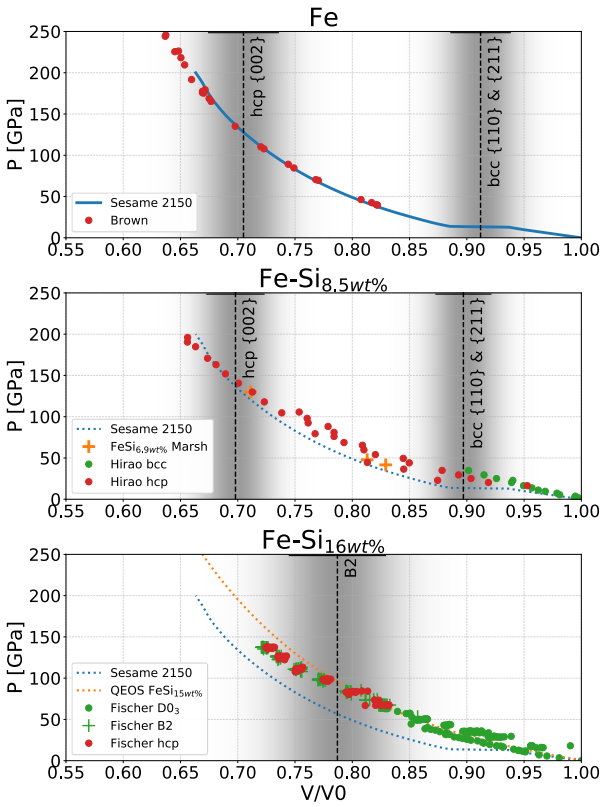

FIG. 4. Pressure-volume relations for iron, Fe-Si$_{8.5\text{wt\%}}$, and Fe-Si$_{16\text{wt\%}}$. Black lines/gray shading show volume and uncertainty of our measurements. In (a), the Sesame 2150 Hugoniot with data from Brown et al.[65]; (b), 300 K Fe-Si$_{8.7\text{wt\%}}$ static compression data[20] and Hugoniot data for Fe-Si$_{6.9\text{wt\%}}$[64]; (c), static compression data for Fe-Si$_{16\text{wt\%}}$[17] between 300-2200 K. (b) and (c) also show the Sesame 2150 Hugoniot.

the relative enthalpy of the main phases at the GGA-PBE approximation level[66] for the exchange-correlation energy functional. These concentrations approximate the experimental conditions while managing calculation size. Non-magnetic B2 and hcp phases use the larger $Fe_{10}Si_4$ cell; ferromagnetic $D0_3$ uses the smaller Fe_5Si_2 cell due to heavier computational cost of magnetic calculations. Magnetic effects are implemented using a standard collinear spin-polarization model. Crystal structure predictions were made with the Ab Initio Random Structure Search[73] code coupled with efficiency enhancements described in Supplementary Material[47] and detailed separately[68].

Figure 5 shows DFT-predicted enthalpy vs. pressure – the lowest enthalpy structure is considered thermodynamically stable. For Fe-Si$_{9.1\text{wt\%}}$, the ferromagnetic bcc phase dominates at low pressures, while hcp is most stable above $\sim$40 GPa. For Fe-Si$_{16.7\text{wt\%}}$, ferromagnetic $D0_3$ phase dominates at low pressures. Starting at $\sim$60 GPa, the B2 phase stabilizes, with the hcp phase slightly less stable than B2 (by 20-50 meV/atom). The fcc phase remains metastable at all pressures in both alloys. The increasing cubic phase stabilization for increasing Si concentration (Fig. 5) agrees with pre-

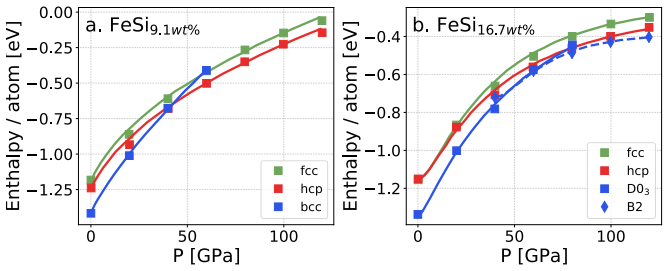

FIG. 5. Phase stability calculations using density functional theory at 0 K for Fe-$Si_{9.1wt\%}$ (a) and Fe-$Si_{16.7wt\%}$ (b).

vious results[12,16,19] and our measurements on the point that small differences in Si concentration impact phase stability, in particular in the range ∼3 - ∼20 wt% of critical interest in planetary science.. This also highlights an advantage of using laser-driven compression, which is largely immune to diffusive concentration changes due to the timescale.

The different experimental timescales provides insight into the apparent inconsistencies across different reports. Our findings agree with Wicks et al.[18], suggesting that the process required to form the hcp phase observed by Fischer in Fe-$Si_{16wt\%}$ does not occur on the 1-10 nanosecond timescale. DAC experiments typically occur on multi-second timescales enabling diffusive processes. While atomic rearrangement also occurs in dynamic compression due to plasticity, phase transformations, etc., bulk alloy concentration changes through diffusion are generally prohibited, though, recent dynamic compression studies have revealed diffusive phase transformations active on tens of nanosecond timescales[33]. In our case, the rapid stabilization of the hcp structure for iron and for Fe-$Si_{8.5wt\%}$, but not for Fe-$Si_{16wt\%}$, may imply that in this latter case the formation of hcp phase requires non-Martensitic action like diffusive de-mixing.

ACKNOWLEDGMENTS

The XFEL experiments were performed at the BL3 of SACLA with the approval of the Japan Synchrotron Radiation Research Institute (proposal nos. 2015A8023, 2015A8066, 2015B8014, 2015B8063, and 2017A8062). This work is in part supported by the French Agence Nationale de la Recherche with the ANR IRONFEL 12-PDOC-0011, by the Japan Society for the Promotion of Science (JSPS) KAKENHI (grant nos. 16H01119 and 18H04368), JSPS core-to-core program on International Alliance for Material Science in Extreme States with High Power Laser and XFEL, the X-ray Free Electron Laser Priority Strategy Program at Osaka University from the Ministry of Education, Culture, Sports, Science, and Technology (contract no. 12005014), the Centre National de la Recherche Scientifique GoToXFEL program, and under the auspices of the Lawrence Livermore National Security, LLC, (LLNS) under Contract No. DE-AC52-07NA27344. This work was supported by the Department of Energy, Laboratory Directed Research and Development program at SLAC National Accelerator Laboratory, under contract DE-AC02-76SF00515 and as part of the Panofsky Fellowship awarded to E.E.M. This work was further supported by Fusion Energy Sciences FWP10018. This project has also received funding from the European Research Council (ERC) under the European Union's Horizon 2020 research and innovation program (grant agreement No. 670787 D PLANETDIVE). DA has received funding from the European Research Council (ERC) under the European Union's Horizon 2020 research and innovation Programme (grant agreement No. 724690). We thank I. Estève for assistance with the scanning electron microscopy and B. Baptiste for assistance with the laboratory X-ray diffraction, that both allowed full characterization of the initial samples. We would like to thank A. Benuzzi-Mounaix, E. Edmund, G. Morard, and C. Wehrenberg for helpful discussions and A. Faenov, T. Pikuz, and Y. Tange for supporting the project.

* krygier1@llnl.gov

[1] L. M. Barker and R. E. Hollenbach, Journal of Applied Physics **45**, 4872 (1974).
[2] D. H. Kalantar, J. F. Belak, G. W. Collins, J. D. Colvin, H. M. Davies, J. H. Eggert, T. C. Germann, J. Hawreliak, B. L. Holian, K. Kadau, P. S. Lomdahl, H. E. Lorenzana, M. a. Meyers, K. Rosolankova, M. S. Schneider, J. Sheppard, J. S. Stölken, and J. S. Wark, Physical Review Letters **95**, 075502 (2005).
[3] S. Tateno, K. Hirose, Y. Ohishi, and Y. Tatsumi, Science **330**, 359 (2010).
[4] A. E. Gleason and W. L. Mao, Nature Geoscience **6**, 571 (2013).
[5] R. F. Smith, J. H. Eggert, D. C. Swift, J. Wang, T. S. Duffy, D. G. Braun, R. E. Rudd, D. B. Reisman, J.-P. Davis, M. D. Knudson, and G. W. Collins, Journal of Applied Physics **114**, 223507 (2013).
[6] R. G. Kraus, R. J. Hemley, S. J. Ali, J. L. Belof, L. X. Benedict, J. Bernier, D. Braun, R. E. Cohen, G. W. Collins, F. Coppari, M. P. Desjarlais, D. Fratanduono, S. Hamel, A. Krygier, A. Lazicki, J. Mcnaney, M. Millot, P. C. Myint, M. G. Newman, J. R. Rygg, D. M. Sterbentz, S. T. Stewart, L. Stixrude, D. C. Swift, C. Wehrenberg, and J. H. Eggert, Science **375**, 202 (2022).
[7] V. Malavergne, P. Cordier, K. Righter, F. Brunet, B. Zanda, A. Addad, T. Smith, H. Bureau, S. Surblé, C. Raepsaet, E. Charon, and R. H. Hewins, Earth and Planetary Science Letters **394**, 186 (2014).
[8] N. L. Chabot, E. A. Wollack, R. L. Klima, and M. E. Minitti, Earth and Planetary Science Letters **390**, 199 (2014).
[9] R. Caracas and R. Wentzcovitch, Geophysical Research Letters

31, L20603 (2004).
[10] D. Antonangeli, J. Siebert, J. Badro, D. L. Farber, G. Fiquet, G. Morard, and F. J. Ryerson, Earth and Planetary Science Letters **295**, 292 (2010).
[11] Z. Mao, J.-F. Lin, J. Liu, A. Alatas, L. Gao, J. Zhao, and H.-K. Mao, Proceedings of the National Academy of Sciences **109**, 10239 (2012).
[12] E. Edmund, G. Morard, M. A. Baron, A. Rivoldini, S. Boccato, K. Hirose, A. Pakhomova, and D. Antonangeli, Nature Communications **13**, 387 (2022).
[13] S. Yue, Y. Li, Q. Yang, K. Zhang, and C. Zhang, IEEE Transactions on Magnetics **55**, 1 (2019).
[14] E. Edmund, D. Antonangeli, F. Decremps, F. Miozzi, G. Morard, E. Boulard, A. Clark, S. Ayrinhac, M. Gauthier, M. Morand, and M. Mezouar, Journal Geophysical Research: Solid Earth **124**, 3436 (2019).
[15] I. Ohnuma, S. Abe, S. Shimenouchi, T. Omori, R. Kainuma, and K. Ishida, ISIJ International **52**, 540 (2012).
[16] R. A. Fischer, A. J. Campbell, R. Caracas, D. M. Reaman, P. Dera, and V. B. Prakapenka, Earth and Planetary Science Letters **357-358**, 268 (2012).
[17] R. A. Fischer, A. J. Campbell, D. M. Reaman, N. A. Miller, D. L. Heinz, P. Dera, and V. B. Prakapenka, Earth and Planetary Science Letters **373**, 54 (2013).
[18] J. K. Wicks, R. F. Smith, D. E. Fratanduono, F. Coppari, R. G. Kraus, M. G. Newman, J. R. Rygg, J. H. Eggert, and T. S. Duffy, Science Advances **4** (2018).
[19] E. Edmund, D. Antonangeli, F. Decremps, G. Morard, S. Ayrinhac, M. Gauthier, E. Boulard, M. Mezouar, M. Hanfland, and N. Guignot, Physical Review B **100**, 134105 (2019).
[20] N. Hirao, E. Ohtani, T. Kondo, and T. Kikegawa, Physics and Chemistry of Minerals **31**, 329 (2004).
[21] R. A. Morrison, J. M. Jackson, W. Sturhahn, D. Zhang, and E. Greenberg, Journal of Geophysical Research: Solid Earth **123**, 4647 (2018).
[22] E. Edmund, F. Miozzi, G. Morard, E. Boulard, A. Clark, F. Decremps, G. Garbarino, V. Svitlyk, M. Mezouar, and D. Antonangeli, Minerals **10**, 98 (2020).
[23] A. Belonoshko, N. Skorodumova, A. Rosengren, and B. Johansson, Science **319**, 797 (2008).
[24] C. M. Huntington, J. L. Belof, K. J. M. Blobaum, R. M. Cavallo, N. B. Kostinski, B. R. Maddox, H.-S. Park, C. Plechaty, S. T. Prisbrey, R. Rudd, D. W. Swift, R. J. Wallace, S. V. Weber, C. Wehrenberg, M. J. Wilson, and B. A. Remington, AIP Conference Proceedings **1793**, 110007 (2017).
[25] A. Krygier, P. D. Powell, J. M. McNaney, C. M. Huntington, S. T. Prisbrey, B. A. Remington, R. E. Rudd, D. C. Swift, C. E. Wehrenberg, A. Arsenlis, H.-S. Park, P. Graham, E. Gumbrell, M. P. Hill, A. J. Comley, and S. D. Rothman, Phys. Rev. Lett. **123**, 205701 (2019).
[26] G. Morard, S. Boccato, A. D. Rosa, S. Anzellini, F. Miozzi, L. Henry, G. Garbarino, M. Mezouar, M. Harmand, F. Guyot, E. Boulard, I. Kantor, T. Irifune, and R. Torchio, Geophysical Research Letters **45**, 11,074 (2018).
[27] S. Merkel, N. Miyajima, D. Antonangeli, G. Fiquet, and T. Yagi, Journal of Applied Physics **100**, 0 (2006).
[28] R. G. Kraus, J.-P. Davis, C. T. Seagle, D. E. Fratanduono, D. C. Swift, J. L. Brown, and J. H. Eggert, Phys. Rev. B **93**, 134105 (2016).
[29] A. Dewaele, A. B. Belonoshko, G. Garbarino, F. Occelli, P. Bouvier, M. Hanfland, and M. Mezouar, Physical Review B **85**, 214105 (2012).
[30] H. Okamoto, Journal of Phase Equilibria **13**, 543 (1992).
[31] J. Verhoogen, Philosophical Transactions of the Royal Society of London. Series A, Mathematical and Physical Sciences **258**, 276 (1965).
[32] J. R. Rygg, R. F. Smith, A. E. Lazicki, D. G. Braun, D. E. Fratanduono, R. G. Kraus, J. M. McNaney, D. C. Swift, C. E. Wehrenberg, F. Coppari, M. F. Ahmed, M. A. Barrios, K. J. M. Blobaum, G. W. Collins, A. L. Cook, P. D. Nicola, E. G. Dzenitis, S. Gonzales, B. F. Heidl, M. Hohenberger, A. House, N. Izumi, D. H. Kalantar, S. F. Khan, T. R. Kohut, C. Kumar, N. D. Masters, D. N. Polsin, S. P. Regan, C. A. Smith, R. M. Vignes, M. A. Wall, J. Ward, J. S. Wark, T. L. Zobrist, A. Arsenlis, and J. H. Eggert, Review of Scientific Instruments **91**, 043902 (2020).
[33] A. E. Gleason, C. A. Bolme, H. J. Lee, B. Nagler, E. Galtier, D. Milathianaki, J. Hawreliak, R. G. Kraus, J. H. Eggert, D. E. Fratanduono, G. W. Collins, R. Sandberg, W. Yang, and W. L. Mao, Nature Communications **6**, 8191 (2015).
[34] B. Albertazzi, N. Ozaki, V. Zhakhovsky, A. Faenov, H. Habara, M. Harmand, N. Hartley, D. Ilnitsky, N. Inogamov, Y. Inubushi, T. Ishikawa, T. Katayama, T. Koyama, M. Koenig, A. Krygier, T. Matsuoka, S. Matsuyama, E. McBride, K. P. Migdal, G. Morard, H. Ohashi, T. Okuchi, T. Pikuz, N. Purevjav, O. Sakata, Y. Sano, T. Sato, T. Sekine, Y. Seto, K. Takahashi, K. Tanaka, Y. Tange, T. Togashi, K. Tono, Y. Umeda, T. Vinci, M. Yabashi, T. Yabuuchi, K. Yamauchi, H. Yumoto, and R. Kodama, Science Advances **3**, 1 (2017).
[35] N. J. Hartley, N. Ozaki, T. Matsuoka, B. Albertazzi, A. Faenov, Y. Fujimoto, H. Habara, M. Harmand, Y. Inubushi, T. Katayama, M. Koenig, A. Krygier, P. Mabey, Y. Matsumura, S. Matsuyama, E. E. McBride, K. Miyanishi, G. Morard, T. Okuchi, T. Pikuz, O. Sakata, Y. Sano, T. Sato, T. Sekine, Y. Seto, K. Takahashi, K. A. Tanaka, Y. Tange, T. Togashi, Y. Umeda, T. Vinci, M. Yabashi, T. Yabuuchi, K. Yamauchi, and R. Kodama, Applied Physics Letters **110**, 071905 (2017).
[36] E. E. McBride, A. Krygier, A. Ehnes, E. Galtier, M. Harmand, Z. Konôpková, H. J. Lee, H.-P. Liermann, B. Nagler, A. Pelka, M. Rödel, A. Schropp, R. F. Smith, C. Spindloe, D. Swift, F. Tavella, S. Toleikis, T. Tschentscher, J. S. Wark, and A. Higginbotham, Nature Physics (2018).
[37] A. L. Coleman, M. G. Gorman, R. Briggs, R. S. McWilliams, D. McGonegle, C. A. Bolme, A. E. Gleason, D. E. Fratanduono, R. F. Smith, E. Galtier, H. J. Lee, B. Nagler, E. Granados, G. W. Collins, J. H. Eggert, J. S. Wark, and M. I. McMahon, Phys. Rev. Lett. **122**, 255704 (2019).
[38] M. J. MacDonald, E. E. McBride, E. Galtier, M. Gauthier, E. Granados, D. Kraus, A. Krygier, A. L. Levitan, A. J. MacKinnon, I. Nam, W. Schumaker, P. Sun, T. B. van Driel, J. Vorberger, Z. Xing, R. P. Drake, S. H. Glenzer, and L. B. Fletcher, Applied Physics Letters **116**, 234104 (2020).
[39] C. E. Wehrenberg, D. McGonegle, C. Bolme, A. Higginbotham, A. Lazicki, H. J. Lee, B. Nagler, H.-S. Park, B. A. Remington, R. E. Rudd, M. Sliwa, M. Suggit, D. Swift, F. Tavella, L. Zepeda-Ruiz, and J. S. Wark, Nature **550**, 496 (2017).
[40] B. J. Jensen, G. T. Gray, and R. S. Hixson, Journal of Applied Physics **105** (2009).
[41] N. Amadou, T. de Resseguier, E. Brambrink, T. Vinci, A. Benuzzi-Mounaix, G. Huser, G. Morard, F. Guyot, K. Miyanishi, N. Ozaki, R. Kodama, and M. Koenig, Physical Review B **93**, 214108 (2016).
[42] C. Langrand, D. Andrault, S. Durand, Z. Konôpková, N. Hilairet, C. Thomas, and S. Merkel, Nature Communications **10**, 5680 (2019).
[43] T. Ishikawa, H. Aoyagi, T. Asaka, Y. Asano, N. Azumi, T. Bizen, H. Ego, K. Fukami, T. Fukui, Y. Furukawa, S. Goto, H. Hanaki, T. Hara, T. Hasegawa, T. Hatsui, A. Higashiya, T. Hirono, N. Hosoda, M. Ishii, T. Inagaki, Y. Inubushi, T. Itoga, Y. Joti,

M. Kago, T. Kameshima, H. Kimura, Y. Kirihara, A. Kiyomichi, T. Kobayashi, C. Kondo, T. Kudo, H. Maesaka, X. M. Marechal, T. Masuda, S. Matsubara, T. Matsumoto, T. Matsushita, S. Matsui, M. Nagasono, N. Nariyama, H. Ohashi, T. Ohata, T. Ohshima, S. Ono, Y. Otake, C. Saji, T. Sakurai, T. Sato, K. Sawada, T. Seike, K. Shirasawa, T. Sugimoto, S. Suzuki, S. Takahashi, H. Takebe, K. Takeshita, K. Tamasaku, H. Tanaka, R. Tanaka, T. Tanaka, T. Togashi, K. Togawa, A. Tokuhisa, H. Tomizawa, K. Tono, S. Wu, M. Yabashi, M. Yamaga, A. Yamashita, K. Yanagida, C. Zhang, T. Shintake, H. Kitamura, and N. Kumagai, Nature Photonics **6**, 540 (2012).

[44] K. Tono, Y. Inubushi, M. Yabashi, H. Tanaka, K. Tiedtke, and A. Azima, New Journal of Physics **15**, 083035 (2013).

[45] Y. Inubushi, T. Yabuuchi, T. Togashi, K. Sueda, K. Miyanishi, Y. Tange, N. Ozaki, T. Matsuoka, R. Kodama, T. Osaka, S. Matsuyama, K. Yamauchi, H. Yumoto, T. Koyama, H. Ohashi, K. Tono, and M. Yabashi, Applied Sciences **10** (2020).

[46] A. Dewaele, C. Denoual, S. Anzellini, F. Occelli, M. Mezouar, P. Cordier, S. Merkel, M. Véron, and E. Rausch, Phys. Rev. B **91**, 174105 (2015).

[47] See supplemental material at [url will be inserted by the production group] for additional experimental details, radiation hydrodynamics simulations, and density functional theory calculations.

[48] J. W. Swegle and D. E. Grady, Journal of Applied Physics **58**, 692 (1985).

[49] I. Ohnuma, S. Abe, S. Shimenouchi, T. Omori, R. Kainuma, and K. Ishida, ISIJ International **52**, 540 (2012).

[50] D. Errandonea, D. Santamaría-Perez, A. Vegas, J. Nuss, M. Jansen, P. Rodríguez-Hernandez, and A. Muñoz, Phys. Rev. B **77**, 094113 (2008).

[51] D. Santamaría-Perez, D. Errandonea, A. Vegas, J. Nuss, M. Jansen, P. Rodríguez-Hernández, A. Muñoz, and R. Boehler, Journal of Physics: Conference Series **121**, 022013 (2008).

[52] S. Malviya, R. R. Kinge, N. Kaurav, and R. C. Dixit, AIP Conference Proceedings **2369**, 020133 (2021).

[53] K. Kadau, T. C. Germann, P. S. Lomdahl, and B. L. Holian, Science **296**, 1681 (2002).

[54] K. Kadau, T. C. Germann, P. S. Lomdahl, and B. L. Holian, Phys. Rev. B **72**, 064120 (2005).

[55] K. Kadau, T. C. Germann, P. S. Lomdahl, R. C. Albers, J. S. Wark, A. Higginbotham, and B. L. Holian, Phys. Rev. Lett. **98**, 135701 (2007).

[56] H. Hwang, E. Galtier, H. Cynn, I. Eom, S. H. Chun, Y. Bang, G. C. Hwang, J. Choi, T. Kim, M. Kong, S. Kwon, K. Kang, H. J. Lee, C. Park, J. I. Lee, Y. Lee, W. Yang, S. H. Shim, T. Vogt, S. Kim, J. Park, S. Kim, D. Nam, J. H. Lee, H. Hyun, M. Kim, T. Y. Koo, C. C. Kao, T. Sekine, and Y. Lee, Science Advances **6**, 1 (2020).

[57] D. McGonegle, D. Milathianaki, B. A. Remington, J. S. Wark, and A. Higginbotham, Journal of Applied Physics **118**, 065902 (2015).

[58] D. N. Polsin, D. E. Fratanduono, J. R. Rygg, A. Lazicki, R. F. Smith, J. H. Eggert, M. C. Gregor, B. H. Henderson, J. A. Delettrez, R. G. Kraus, P. M. Celliers, F. Coppari, D. C. Swift, C. A. McCoy, C. T. Seagle, J.-P. Davis, S. J. Burns, G. W. Collins, and T. R. Boehly, Phys. Rev. Lett. **119**, 175702 (2017).

[59] J. A. Hawreliak, B. El-Dasher, H. Lorenzana, G. Kimminau, A. Higginbotham, B. Nagler, S. M. Vinko, W. J. Murphy, T. Whitcher, J. S. Wark, S. Rothman, and N. Park, Physical Review B **83**, 144114 (2011).

[60] R. A. Fischer and A. J. Campbell, American Mineralogist **100**, 2718 (2015).

[61] J. H. Woodhouse, D. Giardini, and X.-D. Li, Geophysical Research Letters **13**, 1549 (1986).

[62] A. Morelli, A. M. Dziewonski, and J. H. Woodhouse, Geophysical Research Letters **13**, 1545 (1986).

[63] D. Antonangeli, S. Merkel, and D. L. Farber, Geophysical Research Letters **33** (2006).

[64] S. P. Marsh, *LASL shock Hugoniot data*, Vol. 5 (Univ of California Press, 1980).

[65] J. M. Brown, J. N. Fritz, and R. S. Hixson, Journal of Applied Physics **88**, 5496 (2000).

[66] J. P. Perdew, K. Burke, and M. Ernzerhof, Phys. Rev. Lett. **77**, 3865 (1996).

[73] C. J. Pickard and R. J. Needs, Journal of Physics: Condensed Matter **23**, 053201 (2011).

[68] G. Mogni, private communication (2020).

[69] X. Daura, K. Gademann, B. Jaun, D. Seebach, W. F. van Gunsteren, and A. E. Mark, Angewandte Chemie International Edition **38**, 236 (1999).

[70] G. A. Gallet and F. Pietrucci, The Journal of Chemical Physics **139**, 074101 (2013).

[71] H. K. Mao, Y. Wu, L. C. Chen, J. F. Shu, and A. P. Jephcoat, Journal of Geophysical Research **95**, 21737 (1990).

[72] P. Giannozzi, S. Baroni, N. Bonini, M. Calandra, R. Car, C. Cavazzoni, D. Ceresoli, G. L. Chiarotti, M. Cococcioni, I. Dabo, A. D. Corso, S. de Gironcoli, S. Fabris, G. Fratesi, R. Gebauer, U. Gerstmann, C. Gougoussis, A. Kokalj, M. Lazzeri, L. Martin-Samos, N. Marzari, F. Mauri, R. Mazzarello, S. Paolini, A. Pasquarello, L. Paulatto, C. Sbraccia, S. Scandolo, G. Sclauzero, A. P. Seitsonen, A. Smogunov, P. Umari, and R. M. Wentzcovitch, Journal of Physics: Condensed Matter **21**, 395502 (2009).

[73] C. J. Pickard and R. J. Needs, Journal of Physics: Condensed Matter **23**, 053201 (2011).

[74] P. Giannozzi, O. Andreussi, T. Brumme, O. Bunau, M. B. Nardelli, M. Calandra, R. Car, C. Cavazzoni, D. Ceresoli, M. Cococcioni, N. Colonna, I. Carnimeo, A. D. Corso, S. de Gironcoli, P. Delugas, R. A. DiStasio, A. Ferretti, A. Floris, G. Fratesi, G. Fugallo, R. Gebauer, U. Gerstmann, F. Giustino, T. Gorni, J. Jia, M. Kawamura, H.-Y. Ko, A. Kokalj, E. Küçükbenli, M. Lazzeri, M. Marsili, N. Marzari, F. Mauri, N. L. Nguyen, H.-V. Nguyen, A. O. de-la Roza, L. Paulatto, S. Poncé, D. Rocca, R. Sabatini, B. Santra, M. Schlipf, A. P. Seitsonen, A. Smogunov, I. Timrov, T. Thonhauser, P. Umari, N. Vast, X. Wu, and S. Baroni, Journal of Physics: Condensed Matter **29**, 465901 (2017).

[75] R. M. More, K. H. Warren, D. A. Young, and G. B. Zimmerman, The Physics of Fluids **31**, 3059 (1988).

Supplementary Materials for X-ray diffraction study on phase transformation dynamics of iron and Fe-Si alloys along the shock Hugoniot using an x-ray free electron laser

A. Krygier,[1,2,*] M. Harmand,[1] B. Albertazzi,[3] E. E. McBride,[4,5] K. Miyanishi,[6,7] D. Antonangeli,[1] Y. Inubushi,[7,8] R. Kodama,[6,9] M. Koenig,[3,9] T. Matsuoka,[10] G. Mogni,[1] F. Pietrucci,[1] A. M. Saitta,[1] T. Togashi,[7,8] Y. Umeda,[9] T. Vinci,[3] M. Yabashi,[7,8] T. Yabuuchi,[7,8] G. Fiquet,[1] and N. Ozaki[6,9]

[1]*Sorbonne Université, Muséum National d'Histoire Naturelle, UMR CNRS 7590, Institut de Minéralogie, de Physique des Matériaux, et de Cosmochimie (IMPMC), 75005 Paris, France*
[2]*Lawrence Livermore National Laboratory, 7000 East Ave, Livermore, CA 94550, USA*
[3]*LULI, CNRS, CEA, Sorbonne Université, Ecole Polytechnique, Institut Polytechnique de Paris, F-91120 Palaiseau cedex, France*
[4]*European XFEL GmbH, Holzkoppel 4, D-22869 Schenefeld, Germany*
[5]*SLAC National Accelerator Laboratory, 2575 Sand Hill Road, MS 19, Menlo Park, California 94025, USA*
[6]*Institute for Laser Engineering, Osaka University, Suita, Osaka 565-0871, Japan*
[7]*RIKEN Spring-8 Center, Sayo, Hyogo 679-5148, Japan*
[8]*Japan Synchrotron Radiation Research Institute, Sayo, Hyogo 679-5198, Japan*
[9]*Graduate School of Engineering, Osaka University, Suita, Osaka 565-0871, Japan*
[10]*Open and Transdisciplinary Research Initiatives, Osaka University, Suita, Osaka 565-0871, Japan*

(Dated: May 23, 2022)

EXPERIMENTAL DETAILS

We performed powder X-ray diffraction measurements of Fe, Fe-$Si_{8.5wt\%}$, and Fe-$Si_{16wt\%}$ sandwich layered samples. A 10 μm Parylene-N (CH) layer is used as an ablator. A second 200 nm thick Ta layer, prevents pre-heating from the laser-ablator interaction. The $\sim$ 3 μm Fe(-Si_x) sample layer is deposited using physical vapor deposition directly onto the 25 μm thick c-cut single crystal sapphire layer, which is used as a tamper.

While a robust sample, XFEL, and drive laser alignment procedure has been developed, we confirmed alignment using a simple procedure. In some samples, the rear-facing (rear) side of the sapphire window was coated with a $\sim$ 100 nm thick Au layer. The Au layer melts when exposed to the unattenuated XFEL beam; the melted Au region has different optical characteristics and can be readily identified in the imaging alignment cameras, allowing us to confirm the XFEL intersects the region of sample that is driven during the dynamic compression.

The samples have been characterized by ambient diffraction performed using a Rigaku diffractometer and coupled ion polishing and SEM microscopy - a summary of these ambient properties is given in Table S1. Fe and Fe-$Si_{8.5wt\%}$ are observed to take the bcc structure under ambient conditions while Fe-$Si_{16wt\%}$ samples take the B2 structure as indicated by the presence of $\{111\}$ and $\{210\}$ reflections in addition to the bcc reflections.

High pressure was achieved dynamically via laser-generated shock wave using the EH5 end station at SACLA. Our samples were irradiated with $\sim$ 10 J of 532 nm radiation in a 3.4 ns pulse focused with a lens to a $\sim$ 250 x 500 μm^2 spot projected onto the angled target plane. The laser was incident at an angle of $\sim 57^\circ$ from normal giving a target-plane irradiance of $\sim 1 \times 10^{12}$ W/cm^2. The laser interacts with the ablator layer, launching a shock wave into the sample; the difference in shock impedance at the CH and Ta interfaces causes a significant pressure increase in the Ta that propagates to the probe layer. Sapphire has similar shock impedance as Fe and is used to minimize wave reflections at the interface.

Sample	ρ_0 [g/cm^3]	phase	Δz [μm]	Si wt%
Fe	7.86	bcc	3.0	–
Fe-$Si_{8.5wt\%}$	7.37	bcc	2.7	8.5(5)
Fe-$Si_{16wt\%}$	7.08	B2	2.9	16.0(2)

TABLE S1. Summary of sample initial conditions. The density (ρ_0) is calculated from the weighted average of observed diffraction lines corresponding to the cubic phase. Δz is the measured sample thickness.

We probed the crystal lattice structure with X-ray diffraction by using the $\sim$ 10 fs SACLA XFEL pulse, with 10^{11} photons/pulse tuned to 10.1 keV. Scattered X-rays were collected using a 3.2 megapixel CCD detector placed 76.6 mm from the interaction point with a vertical orientation as shown in figure 1 (main text). The sample was probed in a reflection geometry with the X-ray pulse incident on the rear surface at 20° from the sample surface. With respect to the geometry shown in figure 1 i(main text), the X-ray pulse is slitted to 200 μm in the out of the page direction and focused with Kirkpatrick-Baez mirrors to 13 μm in the vertical direction, projecting to $\sim$38 x 200 μm^2 on the sample surface. The detector position is determined with CeO_2 powder diffraction; the detector position calibration and integrations were performed using Dioptas[1]. The reported uncertainty in reflection positions is determined by the width of the best-fit Gaussian to the deconvolution of the ambient and driven reflections.

The synchronization of the main optical beam with the XFEL beam was performed in the same way as described by Albertazzi, et al.[2] and whose dynamics are discussed by Hartley, et al.[3] The coarse timing is tuned with a photodiode

that measures emission from a polyimide sample. Fine tuning is accomplished with a 500 nm thick polycrystalline Au sample. The timing baseline, i.e., zero probe delay, is defined as the time when the diffraction from the Au sample begins to broaden due to sample heating.

XRD SUMMARY TABLE

Table S2 summarizes the shown data. Volume is calculated assuming hydrostaticity and hcp-phase c/a ratio of 1.61, following other shock experiments[4] and close to that reported by static studies[5].

TABLE S2. XRD measurement summary.

Sample	phase	reflection	Q [Å^{-1}]	v/v$_0$
iron	bcc	{110}	3.19 (0.03)	0.912 (0.026)
		{211}	5.57 (0.08)	
	hcp	{002}	3.42 (0.05)	0.705 (0.031)
Fe-Si$_{8.5wt\%}$	bcc	{110}	3.24 (0.03)	0.897 (0.024)
		{211}	5.59 (0.06)	
	hcp	{002}	3.44 (0.04)	0.698 (0.025)
Fe-Si$_{16wt\%}$	B2	{110}	3.40 (0.06)	0.787 (0.042)
		{211}	5.88 (0.11)	

PRESSURE CONSTRAINT

We constrain pressure in our experiments in several ways. First, we have performed accompanying experiments using CH and Al layers, both of which have well constrained equations of state and Hugoniot relations. Here, we have directly measured the velocity at the Al surface, which determines the pressure on the principle Hugoniot. Using impedance matching, we then know the pressure in the ablator, which we can then use to calculate the corresponding pressure in iron. Because the laser pulse is repeatable and other aspects of the experiment are held constant, we

We also constrain pressure using radiation-hydrodynamic simulations described in the next section. A critical aspect of these simulations is that the 1D geometry does not properly model the spatially varying laser focus, or transverse radiation transport out of the ablation plasma, due to the reduced dimensionality. This is typically accounted for by adjusting the laser power with a "power factor" that is optimized by matching predicted and measured velocities and breakout times.

RADIATION-HYDRODYNAMIC SIMULATIONS

Simulations are performed with the incident laser pulse profile and measured target layers. Figure S1 shows the simulated pressure as a function of time and Lagrangian space for peak irradiance of 8×10^{11} W/cm^2. We find a good match for a lower irradiance than used in the experiment, which is typical for 1D simulations. The location of the CH, Fe, and sapphire layers are indicated on the bottom. We used the SESAME 2150 equation of state tables[6] for pure Fe and a QEOS[7] equation of state for Fe-Si$_{16wt\%}$. Here we observe a complicated wave interaction due to surface reflections in the multilayer sample. However, the short attenuation length of 10.1 keV X-rays in Fe (7.46 μm) and the oblique probe angle heavily bias our recorded signal to a small volume near the Fe/sapphire interface with $\sim$64% of the signal coming from a depth of 1 μm (normal to the Fe/sapphire interface surface). This is consistent with the lack of gradients or asymmetry seen in the diffraction.

DENSITY FUNCTIONAL THEORY

For each of the $Fe_{10}Si_2$, Fe_5Si_2 and $Fe_{10}Si_4$ crystalline cells, 10,000 random structures have been generated. These random structures were generated with the AIRSS code[8] by imposing a minimum interatomic distance of 1.5 Å and were comprised in the volume range between 7 - 14 Å^3/atom. At each desired pressure, the enthalpy H=U+P$_{ext}\times$ V where U is the internal energy, P$_{ext}$ is the externally-applied pressure, and V is the volume, of the initial random structures was calculated with the Quantum ESPRESSO ab-initio code[9, 10], as a preliminary indication of their likely thermodynamic favorability. The 1% of the structures with the lowest initial enthalpy were selected for further processing. These favorable structures were subsequently clustered using Daura's algorithm[11] (cutoff value of 2.5) based on the PIV metric [12] with a switching function decaying from 0.9 to 0.1 between 1 and 6 Å. This clustering resulted in a few tens of cluster centers: the geometry of such atomic configurations was optimized with a precision better than 1 meV to obtain the final structures and enthalpies. We adopted the following parameters for DFT calculations: PBE exchange-correlation functional, ultra-soft Vanderbilt pseudopotentials, kinetic-energy cutoff = 60 Ry, charge density cutoff = 600 Ry,$8\times8\times8$ k-point grid, and Methfessel-Paxton smearing with width = 0.01 Ry.

The identity of the final relaxed phases was confirmed with three different methods: space group and symmetry assignment using the spglib library[13], enthalpy equivalence between structures, and structure factor comparison calculated using the VESTA crystal visualization software package[14]. The appearance of the crystal structures was also visualized and inspected with VESTA.

* krygier1@llnl.gov

[1] C. Prescher and V. B. Prakapenka, High Pressure Research **7959** (2015), 10.1080/08957959.2015.1059835.

[2] B. Albertazzi, N. Ozaki, V. Zhakhovsky, A. Faenov, H. Habara, M. Harmand, N. Hartley, D. Ilnitsky, N. Inogamov, Y. Inubushi, T. Ishikawa, T. Katayama, T. Koyama, M. Koenig, A. Krygier, T. Matsuoka, S. Matsuyama, E. McBride, K. P.

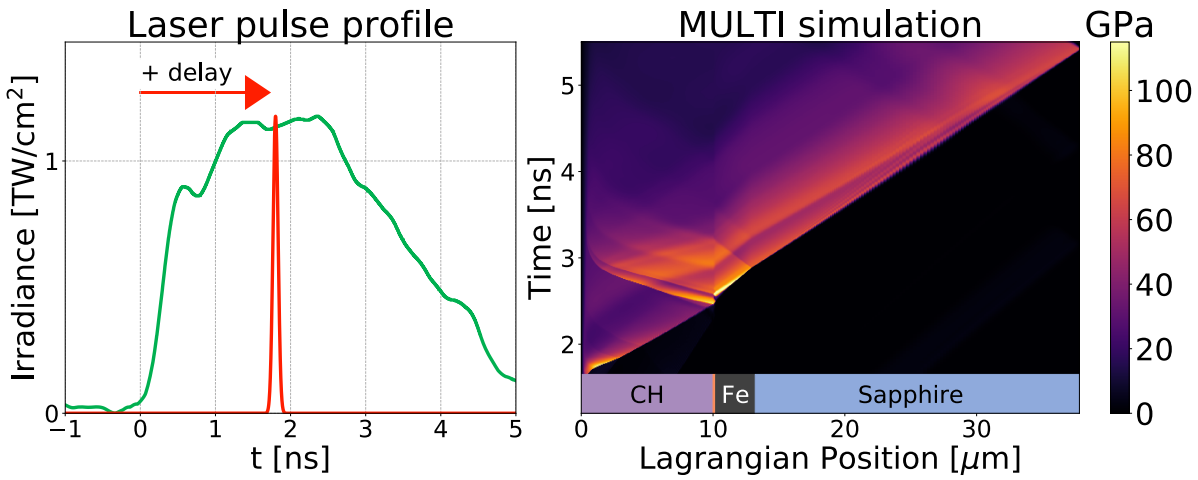

FIG. S1. Experimental pulse shape (left panel) and MULTI hydrodynamics (right panel) simulation showing the pressure as a function of time and Lagrangian position. The peak irradiance is 8×10^{11} W/cm^2, which is lower than our experimental irradiance as typical of 1D radiation hydrodynamics simulations, produces the best fit to our data. The sample layers are indicated on the bottom (with the Ta heat shield included, but not labeled).

Migdal, G. Morard, H. Ohashi, T. Okuchi, T. Pikuz, N. Purevjav, O. Sakata, Y. Sano, T. Sato, T. Sekine, Y. Seto, K. Takahashi, K. Tanaka, Y. Tange, T. Togashi, K. Tono, Y. Umeda, T. Vinci, M. Yabashi, T. Yabuuchi, K. Yamauchi, H. Yumoto, and R. Kodama, Science Advances **3**, 1 (2017).

[3] N. J. Hartley, N. Ozaki, T. Matsuoka, B. Albertazzi, A. Faenov, Y. Fujimoto, H. Habara, M. Harmand, Y. Inubushi, T. Katayama, M. Koenig, A. Krygier, P. Mabey, Y. Matsumura, S. Matsuyama, E. E. McBride, K. Miyanishi, G. Morard, T. Okuchi, T. Pikuz, O. Sakata, Y. Sano, T. Sato, T. Sekine, Y. Seto, K. Takahashi, K. A. Tanaka, Y. Tange, T. Togashi, Y. Umeda, T. Vinci, M. Yabashi, T. Yabuuchi, K. Yamauchi, and R. Kodama, Applied Physics Letters **110**, 071905 (2017).

[4] J. A. Hawreliak, B. El-Dasher, H. Lorenzana, G. Kimminau, A. Higginbotham, B. Nagler, S. M. Vinko, W. J. Murphy, T. Whitcher, J. S. Wark, S. Rothman, and N. Park, Physical Review B **83**, 144114 (2011).

[5] H. K. Mao, Y. Wu, L. C. Chen, J. F. Shu, and A. P. Jephcoat, Journal of Geophysical Research **95**, 21737 (1990).

[6] G. I. Kerley, Sandia Report **SAND93**, 0027 (1993).

[7] R. M. More, K. H. Warren, D. A. Young, and G. B. Zimmerman, The Physics of Fluids **31**, 3059 (1988).

[8] C. J. Pickard and R. J. Needs, Journal of Physics: Condensed Matter **23**, 053201 (2011).

[9] P. Giannozzi, S. Baroni, N. Bonini, M. Calandra, R. Car, C. Cavazzoni, D. Ceresoli, G. L. Chiarotti, M. Cococcioni, I. Dabo, A. D. Corso, S. de Gironcoli, S. Fabris, G. Fratesi, R. Gebauer, U. Gerstmann, C. Gougoussis, A. Kokalj, M. Lazzeri, L. Martin-Samos, N. Marzari, F. Mauri, R. Mazzarello, S. Paolini, A. Pasquarello, L. Paulatto, C. Sbraccia, S. Scandolo, G. Sclauzero, A. P. Seitsonen, A. Smogunov, P. Umari, and R. M. Wentzcovitch, Journal of Physics: Condensed Matter **21**, 395502 (2009).

[10] P. Giannozzi, O. Andreussi, T. Brumme, O. Bunau, M. B. Nardelli, M. Calandra, R. Car, C. Cavazzoni, D. Ceresoli, M. Cococcioni, N. Colonna, I. Carnimeo, A. D. Corso, S. de Gironcoli, P. Delugas, R. A. DiStasio, A. Ferretti, A. Floris, G. Fratesi, G. Fugallo, R. Gebauer, U. Gerstmann, F. Giustino, T. Gorni, J. Jia, M. Kawamura, H.-Y. Ko, A. Kokalj, E. Küçükbenli, M. Lazzeri, M. Marsili, N. Marzari, F. Mauri, N. L. Nguyen, H.-V. Nguyen, A. O. de-la Roza, L. Paulatto, S. Poncé, D. Rocca, R. Sabatini, B. Santra, M. Schlipf, A. P. Seitsonen, A. Smogunov, I. Timrov, T. Thonhauser, P. Umari, N. Vast, X. Wu, and S. Baroni, Journal of Physics: Condensed Matter **29**, 465901 (2017).

[11] X. Daura, K. Gademann, B. Jaun, D. Seebach, W. F. van Gunsteren, and A. E. Mark, Angewandte Chemie International Edition **38**, 236 (1999).

[12] G. A. Gallet and F. Pietrucci, The Journal of Chemical Physics **139**, 074101 (2013).

[13] A. Togo and I. Tanaka, "Spglib: A Software Library for Crystal Symmetry Search," (2018), 1808.01590.

[14] K. Momma and F. Izumi, Journal of Applied Crystallography **44**, 1272 (2011).